First results from the DEAP-3600 dark matter search with argon at SNOLAB

P.-A. Amaudruz,[1] M. Baldwin,[2] M. Batygov,[3] B. Beltran,[4] C. E. Bina,[4] D. Bishop,[1] J. Bonatt,[5] G. Boorman,[6]
M. G. Boulay,[7,5] B. Broerman,[5] T. Bromwich,[8] J. F. Bueno,[4] P. M. Burghardt,[9] A. Butcher,[6] B. Cai,[5] S. Chan,[1]
M. Chen,[5] R. Chouinard,[4] B. T. Cleveland,[10,3] D. Cranshaw,[5] K. Dering,[5] J. DiGioseffo,[5] S. Dittmeier,[1]
F. A. Duncan,[10,3,†] M. Dunford,[7] A. Erlandson,[7,11] N. Fatemighomi,[6] S. Florian,[5] A. Flower,[7,5] R. J. Ford,[10,3]
R. Gagnon,[5] P. Giampa,[5] V. V. Golovko,[11,5] P. Gorel,[4,10,3] R. Gornea,[7] E. Grace,[6] K. Graham,[7] E. Gulyev,[1]
R. Hakobyan,[4] A. Hall,[6] A. L. Hallin,[4] M. Hamstra,[7,5] P. J. Harvey,[5] C. Hearns,[5] C. J. Jillings,[10,3]
O. Kamaev,[11] A. Kemp,[6] M. Kuźniak,[7,5,*] S. Langrock,[3] F. La Zia,[6] B. Lehnert,[7] J. J. Lidgard,[5] C. Lim,[1]
T. Lindner,[1] Y. Linn,[1] S. Liu,[4] P. Majewski,[2] R. Mathew,[5] A. B. McDonald,[5] T. McElroy,[4] T. McGinn,[7,5,†]
J. B. McLaughlin,[5] S. Mead,[1] R. Mehdiyev,[7] C. Mielnichuk,[4] J. Monroe,[6] A. Muir,[1] P. Nadeau,[10,5]
C. Nantais,[5] C. Ng,[4] A. J. Noble,[5] E. O'Dwyer,[5] C. Ohlmann,[1] K. Olchanski,[1] K. S. Olsen,[4] C. Ouellet,[7]
P. Pasuthip,[5] S. J. M. Peeters,[8] T. R. Pollmann,[9,3,5] E. T. Rand,[11] W. Rau,[5] C. Rethmeier,[7] F. Retière,[1]
N. Seeburn,[6] B. Shaw,[1] K. Singhrao,[1,4] P. Skensved,[5] B. Smith,[1] N. J. T. Smith,[10,3] T. Sonley,[10,5]
J. Soukup,[4] R. Stainforth,[7] C. Stone,[5] V. Strickland,[1,7] B. Sur,[11] J. Tang,[4] J. Taylor,[6] L. Veloce,[5]
E. Vázquez-Jáuregui,[12,10,3] J. Walding,[6] M. Ward,[5] S. Westerdale,[7] E. Woolsey,[4] and J. Zielinski[1]
(DEAP-3600 Collaboration)

[1] *TRIUMF, Vancouver, British Columbia, V6T 2A3, Canada*
[2] *Rutherford Appleton Laboratory, Harwell Oxford, Didcot OX11 0QX, United Kingdom*
[3] *Department of Physics and Astronomy, Laurentian University, Sudbury, Ontario, P3E 2C6, Canada*
[4] *Department of Physics, University of Alberta, Edmonton, Alberta, T6G 2R3, Canada*
[5] *Department of Physics, Engineering Physics, and Astronomy,*
Queen's University, Kingston, Ontario, K7L 3N6, Canada
[6] *Royal Holloway University London, Egham Hill, Egham, Surrey TW20 0EX, United Kingdom*
[7] *Department of Physics, Carleton University, Ottawa, Ontario, K1S 5B6, Canada*
[8] *University of Sussex, Sussex House, Brighton, East Sussex BN1 9RH, United Kingdom*
[9] *Department of Physics, Technische Universität München, 80333 Munich, Germany*
[10] *SNOLAB, Lively, Ontario, P3Y 1M3, Canada*
[11] *Canadian Nuclear Laboratories Ltd, Chalk River, Ontario, K0J 1J0, Canada*
[12] *Instituto de Física, Universidad Nacional Autónoma de México, A. P. 20-364, México D. F. 01000, Mexico*

(Dated: May 8, 2018)

This paper reports the first results of a direct dark matter search with the DEAP-3600 single-phase liquid argon (LAr) detector. The experiment was performed 2 km underground at SNOLAB (Sudbury, Canada) utilizing a large target mass, with the LAr target contained in a spherical acrylic vessel of 3600 kg capacity. The LAr is viewed by an array of PMTs, which would register scintillation light produced by rare nuclear recoil signals induced by dark matter particle scattering. An analysis of 4.44 live days (fiducial exposure of 9.87 tonne·days) of data taken during the initial filling phase demonstrates the best electronic recoil rejection using pulse-shape discrimination in argon, with leakage $<1.2\times10^{-7}$ (90% C.L.) between 15 and 31 $\mathrm{keV_{ee}}$. No candidate signal events are observed, which results in the leading limit on WIMP-nucleon spin-independent cross section on argon, $<1.2\times10^{-44}$ cm^2 for a 100 GeV/c^2 WIMP mass (90% C.L.).

PACS numbers: 95.35+d, 29.40.Mc, 26.65.+t, 34.50.Gb, 07.20.Mc, 12.60.Jv

It is well established from astronomical observations that *dark matter* (DM) constitutes most of the matter in the Universe [1], accounting for 26.8% of the energy density, compared to 4.9% for ordinary matter. Weakly Interacting Massive Particles (WIMPs) are one of the leading DM candidates, predicted by a number of theoretical extensions of the Standard Model. Direct detection of WIMPs from the galactic halo is possible via elastic scattering interactions, producing nuclear recoils (NR) of a few tens of keV. Detection requires massive, low-background detectors located deep underground to suppress backgrounds.

This paper reports on the first DM search from DEAP-3600, a liquid argon (LAr) detector which uses single-phase technology, registering only the primary scintillation light from the target medium. This is the first DM search result from a LAr detector, of any technology, exceeding a 1 tonne target mass, and the first such result from a single phase detector, of any target species, at this scale. We emphasize the importance of exceeding the tonne scale: thus far only one technology, liquid Xe TPCs, has achieved 1 tonne fiducial mass while a credible direct detection discovery of DM will require observation in multiple target species. Further, while the WIMP mass reach of collider experiments is limited by beam energy, direct detection experiments are limited only by total exposure, and so a large enough underground detector with sufficiently low backgrounds can access high WIMP mass regions not accessible to colliders. The DEAP-3600 single-phase design offers excellent scalability to ktonne-scale LAr detectors [4, 5].

In this paper we report the best background rejection using pulse-shape discrimination (PSD) in argon at low energy threshold, most relevant for WIMP searches. The PSD uses the substantial difference in LAr scintillation timing between NR and electronic recoils (ER) to reject the dominant β/γ backgrounds [2, 3] at the 10^{-7} level, 4 orders of magnitude beyond that achieved in LXe. This capability will enable a large underground detector using argon to reject the electron backgrounds from solar neutrinos and reach the neutrino floor defined by coherent scattering of atmospheric neutrinos. Employing this PSD, this paper reports a background-free DM search in 9.87 tonne-day exposure, resulting in the best limit on the WIMP-nucleon cross section measured with argon, in the high WIMP mass regime second only to Xe TPC-based searches.

The detector is comprised of an atmospheric LAr target contained in a transparent acrylic vessel (AV) cryostat capable of storing 3600 kg of argon. The AV is viewed by 255 Hamamatsu R5912-HQE photomultiplier tubes (PMTs) operated near room temperature to detect scintillation light from the target. The PMTs are coupled to the AV by 50 cm-long acrylic light guides (LGs). The inner AV surface was coated in-situ with a 3 μm layer of wavelength shifter, 1,1,4,4-tetraphenyl-1,3-butadiene (TPB) to convert 128 nm Ar scintillation light into blue light, which is efficiently transmitted through acrylic. The AV neck is wrapped with optical fibers read out by PMTs, to veto light emission in the AV neck region. The detector is housed in a stainless steel spherical shell immersed in an 8 m diameter ultrapure water tank. All detector materials were selected to achieve the background target of <0.6 events in a 3 tonne-year exposure [5]. To avoid ^{222}Rn/^{210}Pb contamination of the bulk acrylic and the AV-TPB interface, the inner 0.5 mm surface layer of the inner AV was removed in-situ after construction. The Rn exposure was then strictly limited, with the AV and the access glovebox purged with Rn-scrubbed N_2, evacuated and baked before filling. Argon was delivered as cryogenic liquid, stored underground, purified to sub-ppb impurity levels, scrubbed of Rn [6] and liquified in the AV.

PMT signals are decoupled from the high voltage by a set of custom analog signal-conditioning boards, digitized with CAEN V1720 digitizers and handled by the MIDAS DAQ system [7].

The PMT charge response functions are calibrated daily with a system of 22 optical fibres injecting 435 nm light from a pulsed LED. A detailed model for the PMT charge response is used to calculate the mean single photoelectron (SPE) charges, $\langle Q_{SPE}\rangle$ [5, 8]. The combined 3% statistical and systematic uncertainty on $\langle Q_{SPE}\rangle$ is assessed by fitting the measured charge vs. occupancy in calibration data with a simple Poisson model, which allows for the effect of the pedestal biasing the SPE charge fit in the range where the pedestal dominates (below 1 pC, approximately 0.1 PE), as $(1\text{-}\Delta)*\langle Q_{SPE}\rangle$. The difference between the fitted value of Δ and the value predicted by the analytic charge response model in [5] is taken to be the systematic uncertainty arising from the SPE model shape. A full PMT signal simulation is implemented in a detailed Monte Carlo model of the detector, using the GEANT4-based RAT [9]. The simulation uses in-situ measured time vs. charge distributions for noise sources, including late, double, and after-pulsing (AP) for each PMT [5, 8, 10].

The charge of each identified pulse is divided by the PMT-specific mean SPE charge to extract the number of photoelectrons (PEs). $\mathrm{F}_{\mathrm{prompt}}$ is then defined for each event as the ratio of prompt to total charge,

$$\mathrm{F}_{\mathrm{prompt}} \equiv \frac{\sum_{\{i|t_i\in(-28\text{ ns},150\text{ ns})\}} Q_i}{\sum_{\{i|t_i\in(-28\text{ ns},10\ \mu\text{s})\}} Q_i}, \tag{1}$$

where Q_i is the pulse charge in PE and t_i is the pulse time relative to the event time. The relative timing of each channel is calibrated with a fast laser source; the resulting overall time resolution is 1.0 ns. $\mathrm{F}_{\mathrm{prompt}}$ is a powerful PSD variable because it is sensitive to the ratio of excited singlet to triplet states in LAr, with lifetimes of 6 and 1300 ns [11], respectively. This ratio is significantly different for ER and NRs.

The detector trigger was designed to accept all low-energy events above threshold, all high-$\mathrm{F}_{\mathrm{prompt}}$ NRs and to cope with approximately 1 Bq/kg ^{39}Ar activity of LAr [12]. The PMTs signal is continuously integrated in windows 177 ns and 3100 ns wide, from which the prompt energy ($\mathrm{E}_{\mathrm{trigger}}$) and ratio of prompt and wide energies ($\mathrm{F}_{\mathrm{trigger}}$) are calculated. All NR-like triggers with $\mathrm{E}_{\mathrm{trigger}}$ >40 PE, but only 1% of ^{39}Ar-decay-like triggers, are digitized; summary information is recorded for all events. For NR-like events above the analysis PE threshold, the trigger efficiency in the experiment live time is measured to be $(100^{+0.0}_{-0.1})$%, by running in a very low threshold mode. This efficiency is measured after low-level cuts to remove pile-up (Table S1 in Supplemental Material []). For ER-like events the measured trigger efficiency is <100% below 120 PE because of their lower prompt charge.

Stability of the LAr triplet lifetime, τ_3, was verified with a fit accounting for dark noise, TPB fluorescence [13], and PMT AP. From this fit τ_3=1399±20 (PMT syst.)±8 (fit syst.)±6 (TPB syst.)±7(AP syst.) ns, where errors are evaluated by performing the fit separately on individual PMTs, varying the fit range, and varying the TPB fluorescence decay time and times of the AP distributions within uncertainties. This result is consistent with the literature value of 1300±60 ns [11] and is stable throughout the analyzed dataset. See Fig. S1 in Supplemental Material [] for stability over a longer period.

The dominant scintillation event source is ^{39}Ar β decay, resulting in low-F$_{\text{prompt}}$ ERs. In order to define an F$_{\text{prompt}}$ cut constraining the leakage of ^{39}Ar events into the NR band, the F$_{\text{prompt}}$ distribution of ERs and its energy dependence were fitted with an 11-parameter empirical model of F$_{\text{prompt}}$ vs. PE, based on a widened Gamma distribution, $\text{PSD}(n,f) = \Gamma(f;\overline{f}(n),b(n)) \otimes \text{Gauss}(f;\sigma(n))$, where $b(n) = a_0 + \frac{a_1}{n} + \frac{a_2}{n^2}$, $\sigma(n) = a_3 + \frac{a_4}{n} + \frac{a_5}{n^2}$ and $\overline{f}(n)$ is parametrized as $a_6 + \frac{a_7}{n-a_8} + \frac{a_9}{(n-a_{10})^2}$. The 2-dimensional fit of the model to the data (80–260 PE) has χ^2_{ndf} of 5581/(5236-11). Each PE bin in the fit range contributes approximately equally to the overall χ^2 value. As an example, a 1-dimensional slice at 80 PE is shown in Fig. 1(a). The PSD leakage measured in the 120-240 PE window with a 90% NR acceptance is shown in Fig. 1(b). The extrapolated leakage is approximately 10 times lower than projected in the DEAP-3600 design [3]. As further reduction in the PSD leakage is expected from SPE counting [14], the original goal of a 120 PE analysis threshold in 3 years livetime from PSD will likely be surpassed.

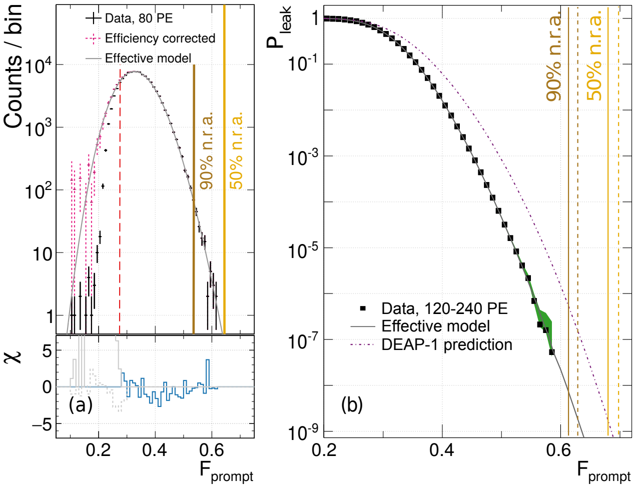

FIG. 1: (a) F$_{\text{prompt}}$ vs. PE distribution slice at 80 PE, with and without the trigger efficiency correction, is shown together with the effective model fit (performed above the red dashed line, indicating the F$_{\text{prompt}}$ value below which the trigger efficiency is <100%). The brown and orange lines correspond to 90% and 50% NR acceptance. (b) Data and model for the 120-240 PE range with 1.87972×10^7 events, represented as leakage probability above a given F$_{\text{prompt}}$ value. A conservative projection from DEAP-1 [3] is also shown with its own NR acceptance lines (all three dashed).

The energy calibration uses internal backgrounds and external radioactive sources. The internal calibration uses β's from ^{39}Ar decay, with an endpoint of 565 keV, which are uniformly distributed in the detector, as WIMP-induced NRs would be. The external calibration uses a ^{22}Na source, which produces 1.27 MeV γ's and a 30-50 keV photo-absorption feature near the AV surface. The simulated spectra of ^{39}Ar and ^{22}Na are fit to the data to find the energy response function relating T$_{\text{eff}}$ [keV$_{\text{ee}}$] (electron-equivalent energy) to detected PE,

$$N_{\text{PE}}(T_{\text{eff}}) = c_0 + c_1 T_{\text{eff}} + c_2 T_{\text{eff}}^2, \tag{2}$$

where c_0=1.2±0.2 PE, c_1=7.68±0.16 PE keV$_{\text{ee}}{}^{-1}$ and c_2=-(0.51±2.0)×10^{-3} PE keV$_{\text{ee}}{}^{-2}$. The offset c_0 is fixed to values returned by analysis of mean pretrigger window charge for each run. The internal and external sources are fit separately, because of different spatial distributions. The ^{39}Ar fit result based on the DM search data constitutes the nominal calibration, while the ^{39}Ar–^{22}Na fit parameter differences, determined from a pair of runs taken just after the 2nd fill (see next page), are combined with the statistical uncertainties and used as systematic uncertainties from position and model depencence on $c_{1,2}$.

The final response function is shown in Fig. 2 together with the ^{39}Ar data spanning from below to above the analysis energy window (see Fig. S2 in Supplemental Material [] for the ^{22}Na fit). The energy response function linear terms, c_1, for ^{39}Ar and ^{22}Na agree within errors. As a cross-check, the response function is extrapolated to compare with high-energy γ lines, see Fig. 2.

The light yield (LY) at 80 PE is 7.80±0.21(fit syst.)±0.22(SPE syst.) PE/keV$_{\text{ee}}$, where the latter uncertainty is from SPE calibration.

A Gaussian energy resolution function is used to smear the spectra in the fit, with variance $\sigma^2 = c_0 + p_1(\text{PE} - c_0)$. The extrapolated resolution at 80 PE from best fit values for ^{39}Ar and ^{22}Na is 20±1% and 21±1%, respectively. A lower bound on the energy resolution at 80 PE is 12% (p_1 = 1.185), determined from counting statistics widened by the measured in-situ SPE charge resolution. Due to the steeply falling WIMP-induced spectrum, broader resolutions imply stronger limits at low WIMP masses. Thus using this lower bound is conservative.

The NR acceptance of the F$_{\text{prompt}}$ cut is determined from a simulation of ^{40}Ar recoils distributed uniformly in LAr. The simulation assumes the quenching factor measured by SCENE [15] at zero electric field, and the triplet/singlet ratio energy dependence required to reproduce the reported median $\mathtt{f}_{90}$ values. The simulation then applies the full response of the detection and analysis chain, which includes all noise components known to affect shape and width of the F$_{\text{prompt}}$ distribution. PMT AP is the dominant effect contributing to shifting F$_{\text{prompt}}$ relative to the intrinsic value [10], with an average AP probability of (7.6±1.9)% [5], approximately

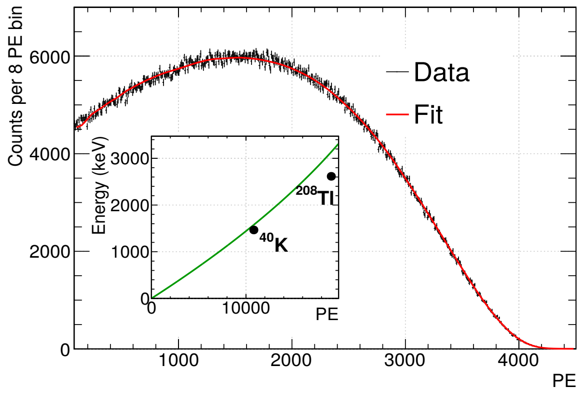

FIG. 2: Measured, trigger-efficiency-corrected ^{39}Ar β spectrum from a subset of the data and the fit function (red) based on simulation, with $\chi^2_{ndf} = 1.02$. The inset shows the global energy reponse function, Eq. (2), from the ^{39}Ar fit, and, as a cross-check, γ lines from ^{40}K and ^{208}Tl compared with the extrapolated function; ^{208}Tl diverges from the function because of PMT and DAQ non-linearity.

5×larger than in SCENE. We note this 7.6% produces a proportional 5% shift in the median $F_{\rm prompt}$. Comparison of external neutron AmBe source data with a simplified detector simulation shows qualitative agreement and serves as a validation of the model, see Fig. S3 in Supplemental Material []. AmBe data is not used directly to model the WIMP-induced NR acceptance as 59% of AmBe events in the 120-240 PE window contain multiple elastic neutron scatters.

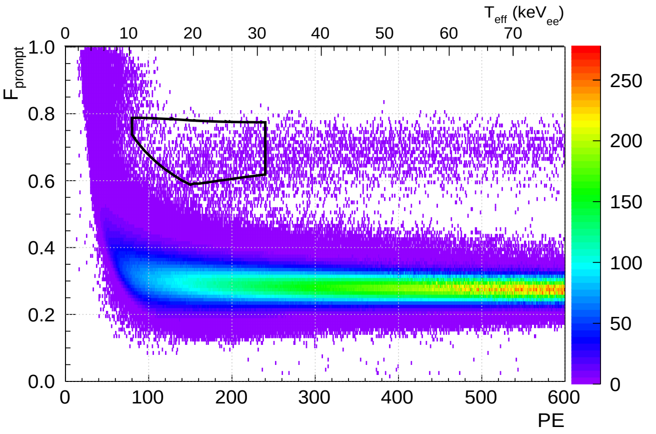

FIG. 3: AmBe source data after cuts, with the ROI for the WIMP search (black box).

The region-of-interest (ROI) in this analysis, as shown in Fig. 3, was defined by allowing for an expectation of 0.2 leakage events from the ^{39}Ar band, determined with the PSD model. It maintains the NR acceptance of >5% at the lowest energies. The smaller number of ^{39}Ar events in the short exposure and the low $F_{\rm prompt}$ leakage allowed us to set the energy threshold at 80 PE (10 keV$_{\rm ee}$), lower than the nominal 120 PE originally projected [3]. Above 150 PE the lower limit on $F_{\rm prompt}$ is chosen to remove 5% of NRs in each bin. The ROI also has a maximum $F_{\rm prompt}$ chosen to remove 1% of NRs in each 1 PE bin. The maximum energy was set to 240 PE to reduce possible backgrounds from the surface α activity [16].

The first LAr fill of the detector took approximately 100 days between May and mid-August 2016. For the majority of this time, Ar gas was introduced into the detector from the purification system for cooling. In the final phase of the fill, shortly following the discussed dataset, a leak in the detector neck contaminated LAr with clean Rn-scrubbed N_2. The detector was subsequently emptied and refilled, and it has been taking data since Nov. 1, 2016, with a slightly lower liquid level.

In this work, we focus on the period Aug. 5 to 15 (9.09 days), when the detector contained a constant LAr mass. The refractive index difference between liquid vs. gaseous Ar is such that scintillation light in the LAr reaching the surface of the liquid with angle of incidence >53° is totally internally reflected. This produces rates in the PMTs facing the gas which are 20% lower than rates of PMTs facing the liquid. Consequently, from the PMT rates the liquid level can be inferred, 590±50 mm above the AV centre, and the full LAr mass: 3322±110 kg.

Calibrations were performed after the 2nd fill: 23 h of ^{22}Na (Nov. 3-4) and 65 h of AmBe data (Dec. 2-4).

Data were analyzed from runs where (1) the difference between the maximum and minimum AV pressures corresponded to <10 mm change in the liquid level and (2) there were no intermittently mis-behaving PMTs, i.e. no PMT read <50% of its average charge, determined from approximately 5 minute samples (all runs with such PMTs were affected by the issue for a large fraction of the run and were thus flagged). Independently, during this dataset one PMT was turned off (and has since returned to operation). In all cases, pressure excursions were correlated with periods of the cryocoolers operating at reduced power. Out of 8.55 d of physics runs, 2.92 d are removed by failing both criteria and an additional 0.91 d by failing criterion 2 alone. The remaining 4.72 d of run time contained a total deadtime of 0.28 d, due to 17.5 μs deadtime after each trigger, resulting in a 4.44 d livetime.

Acceptance for WIMP-induced NR events, see Fig. 4(a), is determined using a combination of ^{39}Ar events (uniformly distributed in the LAr volume) and simulation of $F_{\rm prompt}$ for NRs. The sample of ^{39}Ar single-recoils is obtained first by applying low-level cuts to remove events (1) from DAQ calibration, (2) from pile-up or (3) highly asymmetric (>40% of charge in a single PMT) e.g. Cherenkov events in LGs and PMTs. The approach of measuring acceptance for NRs using ERs is used since none of the cut variables depend on the pulse time information, only $F_{\rm prompt}$ does, which is handled separately. See Table S1 in Supplemental Material [] for a detailed breakdown of the impact of run selection and cuts. The $F_{\rm prompt}$ simulation for NRs is validated by comparison with the AmBe data.

Quality cuts are applied to ^{39}Ar events within the energy window in order to determine the ER acceptance: the event time cut requires that the scintillation peak is positioned early in the waveform (which ensures reliable $F_{\rm prompt}$ evaluation), cuts on the fraction of charge in the brightest PMT and on the neck veto remove high-charge AP triggering the detector as well as light emission in the AV neck (e.g. Cherenkov). We have identified a class of background events originating in the neck region and are characterizing it for future larger-exposure searches.

The fiducial acceptance is determined relative to the events remaining after the quality cuts. Fiducialization in this analysis employs low-level PE ratio cuts. These are that the fraction of scintillation-induced (AP corrected) PE [10, 14]) in the PMT which detects the most light be $<7\%$, and that the fraction of charge in the top 2 rows of PMTs in the detector be $<5\%$. These variables are strongly correlated with the radial and vertical event positions, respectively, and so effectively reject events at the surface of the detector and in the neck. The volume, after cuts on these variables (Table S1 in Supplemental Material []), corresponds roughly to a sphere of radius $\sim$773 mm, truncated at the LAr level at $z\approx590$ mm. The fiducial mass, 2223±74 kg, is determined from the full LAr mass and measured acceptance of the fiducialization cuts. The expected activity of ^{39}Ar contained in this fiducial mass is 2245±198 Bq [12], consistent with the fiducial rate observed in DEAP-3600, 2239±8 Hz.

Position reconstruction algorithms have been tested on the data and will be used to further reduce backgrounds in longer exposure runs. However, in this analysis they were used only as a cross-check (see Fig. S4 in Supplemental Material []).

The main background sources are α activity, neutrons, and leakage from ^{39}Ar and other ERs. As external backgrounds contribution to this early analysis is negligible, we have not yet determined their distributions.

^{222}Rn, ^{218}Po and ^{214}Po α decays are identified in the LAr bulk as well-defined high-energy peaks or based on time delayed coincidence with α-α (^{222}Rn-^{218}Po and ^{220}Rn-^{216}Po) or β-α (^{214}Bi-^{214}Po) tags, resulting in activities: $(1.8\pm0.2)\times10^{-1}$ μBq/kg of ^{222}Rn, $(2.0\pm0.2)\times10^{-1}$ μBq/kg of ^{214}Po, and $(2.6\pm1.5)\times10^{-3}$ μBq/kg of ^{220}Rn. For comparison approximate values from other experiments are: 66 μHz/kg of ^{222}Rn and 10 μHz/kg of ^{220}Rn in LUX [17], 6.57 μBq/kg of ^{222}Rn and 0.41 μBq/kg of ^{220}Rn in PandaX-II [18], and 10 μBq/kg of ^{222}Rn in XENON1T [19]. The activity of ^{214}Po in the bulk is consistent with the earlier part of the chain, indicating that it is mostly mixed within the LAr volume (see Fig. S5 in Supplemental Material []). Out-of-equilibrium ^{210}Po α decays are identified by degraded energies characteristic of α's coming from below the TPB layer. The activity of ^{210}Po is determined with a fit of simulated spectra to the data: 0.22±0.04 mBq/m^2 on the AV surface and <3.3 mBq in the AV bulk, see Fig. S6 in Supplemental Material [].

The dominant source of neutron events is expected to be from (α, n) reactions and spontaneous fission in the PMTs. The PMT borosilicate glass contribution is constrained with measurements of the 2614 keV and 1764 keV γ-rays from the ^{232}Th and ^{238}U decay chains, respectively. Activities of both decay chains seen in-situ agree within a factor of two with a simulation based on the screening results. Neutron backgrounds can also be measured by searching for NRs followed by capture γ's. The efficiency of this technique was calibrated using neutrons from an AmBe source deployed near the PMTs. No neutron candidates were seen in 4.44 d (80–10000 PE window, no fiducial cuts), which is consistent with the assay-based expectation. Systematic uncertainties considered in the WIMP cross section limit calculation include uncertainty on the NR energy response, exposure (from livetime and total LAr mass), and quality and fiducial cut acceptance, see Fig. 4(a). The uncertainty on the NR acceptance of the $F_{\rm prompt}$ cut is determined by varying the simulation inputs: triplet/singlet ratio (within errors propagated from the SCENE [15] measurement of $\mathtt{f}_{90}$), the triplet lifetime uncertainty (70 ns, from the difference between SCENE and this work), and the AP probability. The main uncertainty in the final exclusion curve originates from the NR energy response. This is

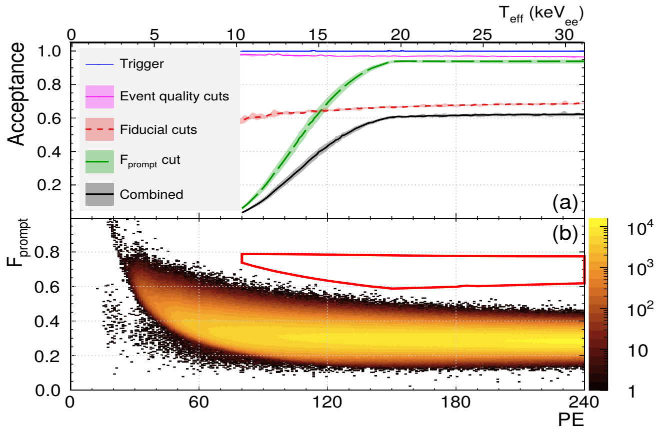

FIG. 4: (a) The acceptance with systematic error bands in the 80–240 PE window. The acceptance is calculated individually for each run and then weighted by livetime, with uncertainties taken as maximum and minimum variations about the weighted mean. Uncertainties on trigger acceptance measurement and $F_{\rm prompt}$ cut acceptance are discussed in the text. (b) $F_{\rm prompt}$ vs. PE for events passing cuts, with the WIMP search ROI (red).

dominated by uncertainties in Eq. (2); the second largest contribution is associated with the NR quenching factor, i.e. the reduction in NR scintillation yield relative to ER ($[\mathrm{keV_r}] = \mathcal{L}_{\mathrm{eff}} \cdot [\mathrm{keV_{ee}}]$, when referring to energies of NR, $\mathrm{keV_r}$, the unit of the full energy of the recoil, can be used). We used measurements from SCENE, which reports two different NR-energy-dependent quenching factors, differing due to non-unitary recombination at null field: $\mathcal{L}_{\mathrm{eff},{}^{83m}\mathrm{Kr}}$ (the ratio of LY measurements for NRs to ^{83m}Kr ER calibration) and $\mathcal{L}$ (the Lindhard-Birks quenching factor describing the suppression of scintillation photons and extracted electrons). We adjusted the Lindhard-Birks quenching factors fit to $\mathcal{L}$ to account for the relative recombination rates of NR and ^{83m}Kr ER at null field, according to the NEST model [20], fitting Thomas-Imel and Doke-Birks recombination parameters to SCENE's $\mathcal{L}_{\mathrm{eff},{}^{83m}\mathrm{Kr}}$ values. The fit uncertainties were inflated to account for differences between the SCENE and DEAP-3600 detectors and the different recombination rates of the ^{83m}Kr ER and the ^{22}Na low-energy feature used for our energy calibration. These factors, along with uncertainty in the SCENE value of Birks' constant and the difference between $\mathcal{L}$ and $\mathcal{L}_{\mathrm{eff},{}^{83m}\mathrm{Kr}}$ were included in the overall quenching factor uncertainty.

No events are observed in the ROI, see Fig. 4(b). Figure 5 shows the resulting upper limit on the spin-independent WIMP-nucleon scattering cross section as a function of WIMP mass, based on the standard DM halo model [21]. A 90% C.L. upper limit is derived employing the Highland-Cousins method [22] (a counting only technique which incorporates systematic uncertainties). For a more conservative limit, the predicted background from ^{39}Ar leakage was not subtracted. We note that this analysis was not blind.

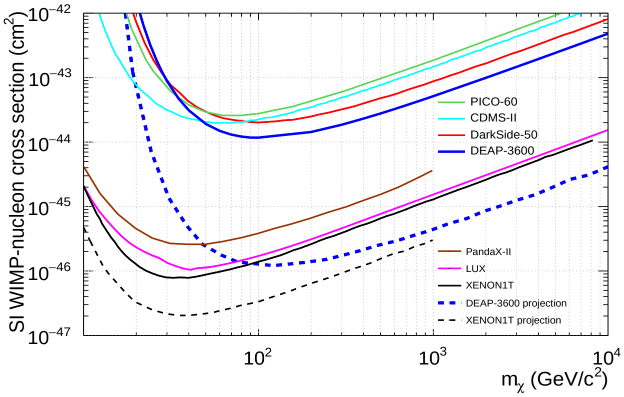

FIG. 5: Spin-independent WIMP-nucleon cross section 90% C.L. exclusion from 4.44 live days of DEAP-3600 data. Also shown are current results from other searches [23–28], and the full sensitivity of XENON1T and DEAP-3600 (a 3 tonne-year background-free exposure with a 15 $\mathrm{keV_{ee}}$ threshold).

DEAP-3600 achieved 7.8 PE/$\mathrm{keV_{ee}}$ LY at the end of the detector fill without recirculation, and demonstrated better-than-expected PSD (permitting a 37 $\mathrm{keV_r}$ energy threshold), with promising α and neutron background levels. Analysis of the first 4.44 d of data results in the best limit at low energies on discrimination of β-decay backgrounds using PSD in LAr at 90% NR acceptance, with measured leakage probability of $<1.2\times10^{-7}$ (90% C.L.) in the energy window 15-31 $\mathrm{keV_{ee}}$ (52-105 $\mathrm{keV_r}$). This measurement has lower threshold than DEAP-1 [3] and higher statistics than DarkSide-50 [26]. After NR selection cuts no events are observed, resulting in the best spin-independent WIMP-nucleon cross section limit measured in LAr [26] of $<1.2\times10^{-44}$ cm^2 for a 100 GeV/c^2 WIMP (90% C.L.)[§]. Data collection has been ongoing since Nov. 2016 and forms the basis for a more sensitive DM search currently in progress.

This work is supported by the Natural Sciences and Engineering Research Council of Canada, the Canadian Foundation for Innovation (CFI), the Ontario Ministry of Research and Innovation (MRI), and Alberta Advanced Education and Technology (ASRIP), Queen's University, University of Alberta, Carleton University, DGAPA-UNAM (PAPIIT No. IA100316 and IA100118) and Consejo Nacional de Ciencia y Tecnología (CONACyT, Mexico, Grant No. 252167), European Research Council (ERC StG 279980), the UK Science & Technology Facilities Council (STFC) (ST/K002570/1), the Leverhulme Trust (ECF-20130496). Studentship support by the Rutherford Appleton Laboratory Particle Physics Division, STFC and SEPNet PhD is acknowledged. We thank SNOLAB and its staff for support through underground space, logistical and technical services. SNOLAB operations are supported by CFI and the Province of Ontario MRI, with underground access provided by Vale at the Creighton mine site. We thank Compute Canada, Calcul Québec and the Center for Advanced Computing at Queen's University for providing the excellent computing resources required to undertake this work.

[†] Deceased.

[*] Electronic address: mkuzniak@physics.carleton.ca

[1] P. A. R. Ade et al. (Planck), Astron. Astrophys. **594**, A13 (2016)
[2] M. G. Boulay, A. Hime, Astropart.Phys. **25**, 179 (2006)
[3] P.-A. Amaudruz et al., Astropart. Phys. **85**, 1 (2016)
[4] M. Kuźniak et al., Nucl. Part. Phys. Proc. **273**, 340 (2016)
[5] P.-A. Amaudruz et al., arXiv:1712.01982 (2017)

[§] During the review process of this paper, new results from DarkSide-50 [29] were announced. DEAP-3600 remains the most sensitive non-Xe search in 45–80 GeV/c^2 mass range.

[6] E. O'Dwyer, M.Sc. thesis, Queen's University, 2011.
[7] T. Lindner (DEAP), J. Phys. Conf. Ser. **664**, 82026 (2015)
[8] P.-A. Amaudruz et al., arXiv:1705.10183 (2017)
[9] T. Caldwell, talk at AARM Meeting, Fermilab, March 19-22 (2014), `https://zzz.physics.umn.edu/lowrad/_media/meeting7/rat_aarm_2014.pdf`
[10] A. Butcher et al., arXiv:1703.06204 (2017)
[11] T. Heindl et al., Europhys. Lett. **91**, 62002 (2010)
[12] P. Benetti et al., Nucl. Instrum. Methods A **574**, 83 (2007)
[13] E. Segreto, Phys. Rev. C **91**, 035503 (2015)
[14] M. Akashi-Ronquest et al., Astropart. Phys. **65**, 40 (2015)
[15] H. Cao et al., Phys. Rev. D **91**, 092007 (2015)
[16] P.-A. Amaudruz et al., Astropart. Phys. **62**, 178 (2015)
[17] A. Bradley et al., Phys. Procedia **61**, 658 (2015)
[18] A. Tan et al., Phys. Rev. D **93**, 122009 (2016)
[19] P. A. Breur, talk at XeSAT 2017, April 3-7, `https://indico.cern.ch/event/573069/sessions/230077/attachments/1440290/2217054/170404_Xesat_Radon_signals_in_XENON1T_presentation_FINAL.pdf`
[20] M. Szydagis et al., JINST **6**, P10002 (2011)
[21] C. McCabe, Phys. Rev. D **82**, 023530 (2010)
[22] R. D. Cousins, V. L. Highland, Nucl. Instrum. Methods A **320**, 331 (1992)
[23] E. Aprile et al., arXiv:1705.06655 (2017)
[24] D. S. Akerib et al., Phys. Rev. Lett. **118**, 021303 (2017)
[25] A. Tan et al., Phys. Rev. Lett. **117**, 121303 (2016)
[26] P. Agnes et al., Phys. Rev. D **93**, 081101 (2016)
[27] R. Agnese et al., Phys. Rev. D **92**, 072003 (2015)
[28] C. Amole et al., Phys. Rev. D **93**, 052014 (2016)
[29] P. Agnes et al., arXiv:1802.07198v1 (2018)

Supplemental Materials: First results from the DEAP-3600 dark matter search with argon at SNOLAB

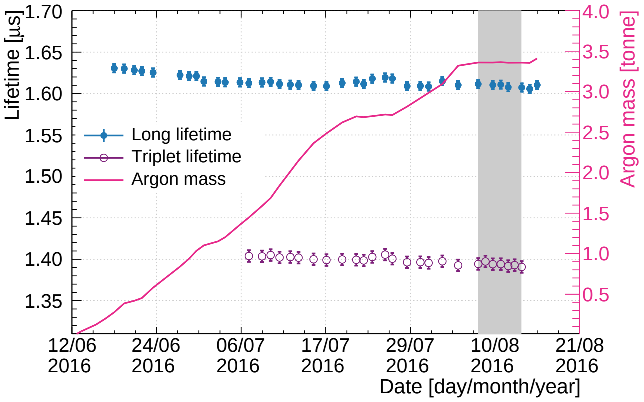

FIG. S1: Stability of late light timing measured during the detector fill. The 'long lifetime' is determined with a simple 'exponential + linear' fit to the summed waveforms from 500 ns to 3000 ns. Such a fit overestimates the triplet lifetime by including effects such as PMT AP and TPB fluorescence in addition to the LAr triplet lifetime. Shown as well is the 'triplet lifetime' extracted from the same pulse shapes with a more elaborate fit that accounts for these effects. At low LAr mass, the averaged pulse shapes include a contribution from gaseous Ar scintillation, which also leads to an increase in the fit lifetimes. The triplet lifetime measurements are shown for a period when a sizable amount of LAr was in the detector. The error bars shown are primarily systematic, as the statistical uncertainties from the fits are smaller than the marker size. LAr was not recirculated or repurified during the fill. The grey shaded area represents the dataset used for the dark matter search presented here. The fit time constant is stable within that period to <1%.

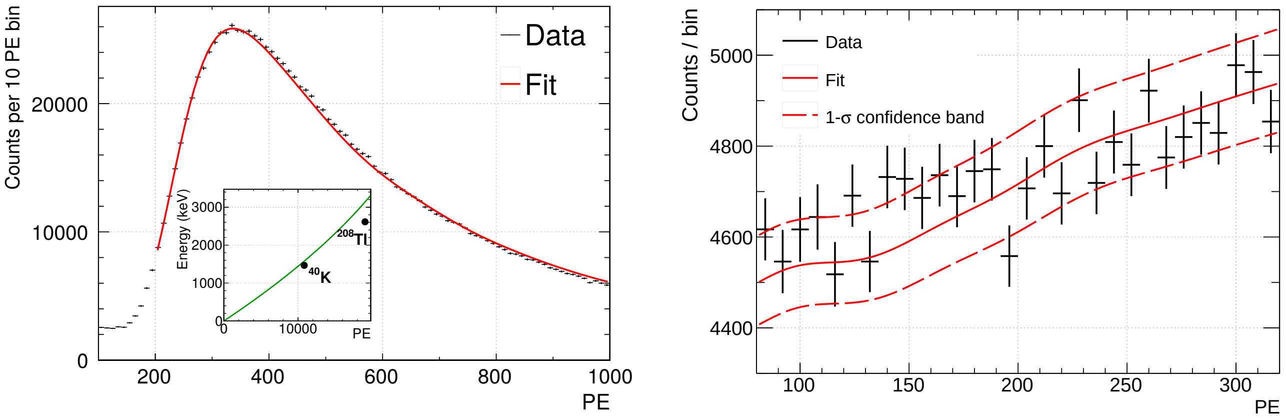

FIG. S2: (a) Spectrum collected after the 2nd detector fill with an external ^{22}Na source overlayed with the fit function (red) based on simulation. The inset shows the global energy reponse function from the ^{39}Ar fit, $N_{\rm PE}(T_{\rm eff}) = c_0 + c_1 {\rm T}_{\rm eff} + c_2 {\rm T}_{\rm eff}{}^2$, with c_0=1.2±0.2 PE, c_1=7.68±0.16 PE keV$_{\rm ee}{}^{-1}$ and c_2=-(0.51±2.0)×10^{-3} PE keV$_{\rm ee}{}^{-2}$. As a cross-check, on the inset γ lines from ^{40}K and ^{208}Tl are compared with the extrapolated function; ^{208}Tl diverges from the function because of PMT and DAQ non-linearity. (b) ^{39}Ar data and fit from Fig. 2 zoomed in to the low energy window, with 1-σ confidence band shown (dashed).

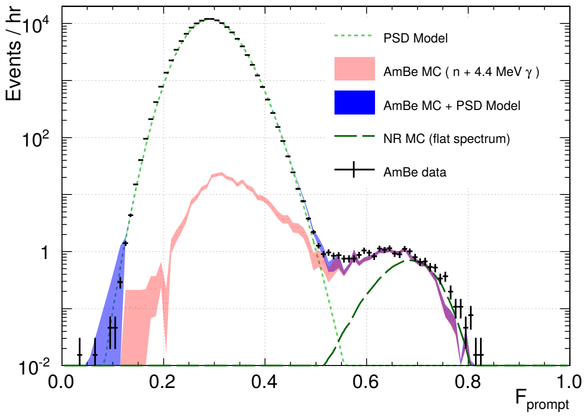

FIG. S3: The F_{prompt} distribution for 140<PE<240 in AmBe calibration data, compared to summed simulated contributions for AmBe neutrons, and 4.4 MeV γ's and the ^{39}Ar F_{prompt} model normalized to the peak of the distribution. Also plotted is the simulation of single scatter nuclear recoils, our proxy for WIMP-induced events, with a flat energy spectrum (see legend). Error bars shown on the simulated distributions are statistical, not systematic. The simulation includes neutrons and 4.4 MeV γ's from the AmBe source and considers scattering- or capture-induced γ's only for neutrons that entered the LAr.

	Cut	Livetime	Acceptance %		#ROI events
run	Physics runs	8.55 d			
	Stable cryocooler	5.63 d			
	Stable PMT	4.72 d			
	Deadtime corrected	4.44 d			119181
low level	DAQ calibration				115782
	Pile-up				100700
	Event asymmetry				787
quality	Max charge fraction per PMT		99.58±0.01		654
	Event time		99.85±0.01		652
	Neck veto		$97.49^{+0.03}_{-0.05}$		23
fiducial	Max scintillation PE fraction per PMT			$75.08^{+0.09}_{-0.06}$	7
	Charge fraction in the top 2 PMT rings			$90.92^{+0.11}_{-0.10}$	0
	Total	4.44 d	96.94±0.03	$66.91^{+0.20}_{-0.15}$	0

TABLE S1: Run selection criteria and cuts with their effects on livetime, integrated acceptance, the fiducial fraction, and the number of events left in the ROI. The acceptance is calculated individually for each run and then weighted by livetime to provide an overall acceptance with the uncertainties taken as maximum and minimum variations about this weighted mean from each run. The fiducial acceptance is determined relative to the events remaining after the quality cuts, which are considered a clean sample of ^{39}Ar β's uniformly distributed in LAr. The total number of triggers before any cuts was 1.38×10^9, with 6.47×10^7 in the 80-240 PE window.

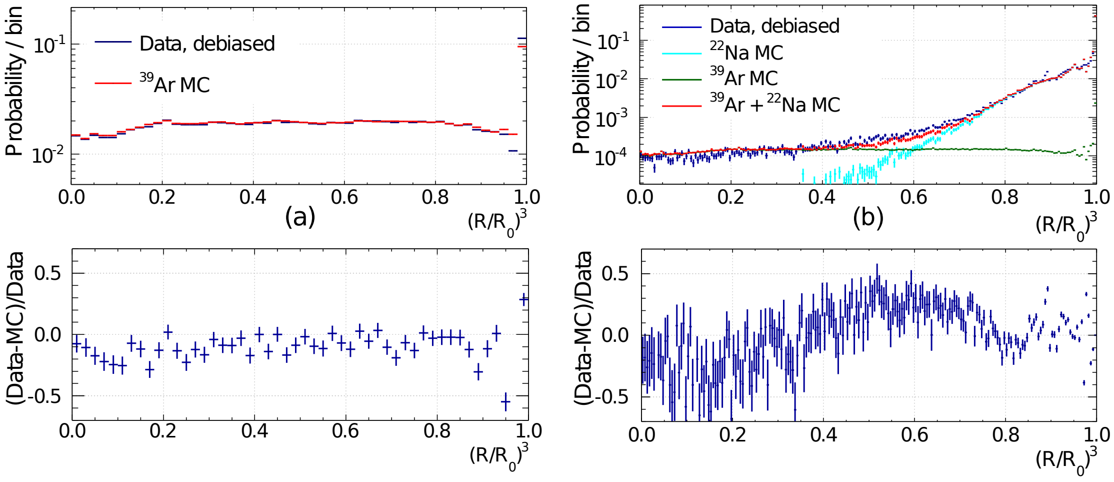

FIG. S4: A maximum likelihood fitter relies on the full Monte Carlo of the detector, including its optical properties, and minimizes the difference between the observed pattern of PMT charges and the one expected based on a distribution constructed from simulation, under the assumption that the illumination of the detector is symmetric around the axis of the event position vector. Residual position bias is corrected for using the uniformly distributed population of ^{39}Ar β's. To study the reconstruction of events from the inner AV surface, as expected for α backgrounds, we apply the ^{39}Ar-derived calibration to ^{22}Na events, which are strongly peaked near the surface. Reconstructed radii of (left) ^{39}Ar uniformly distributed in the detector and (right) tagged events from an external ^{22}Na calibration source after correcting for radial bias in data (blue), ^{22}Na Monte Carlo (cyan), distribution of random coincidences of the source tag with ^{39}Ar decays (green) and the sum of both ^{39}Ar and ^{22}Na distributions (red). Residuals are displayed in the bottom row, showing qualitative agreement.

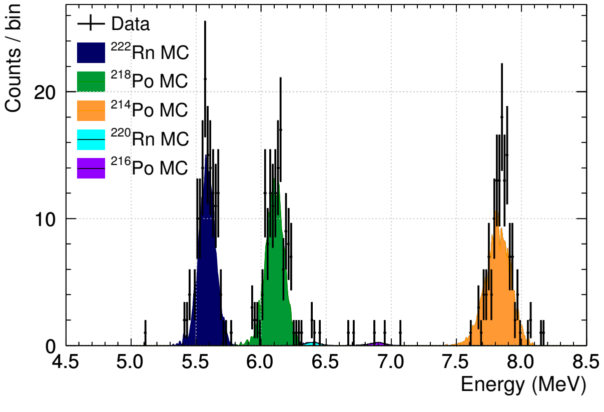

FIG. S5: Peaks from tagged alphas in ^{222}Rn and ^{220}Rn chains in the detector data overlayed with Monte Carlo distributions.

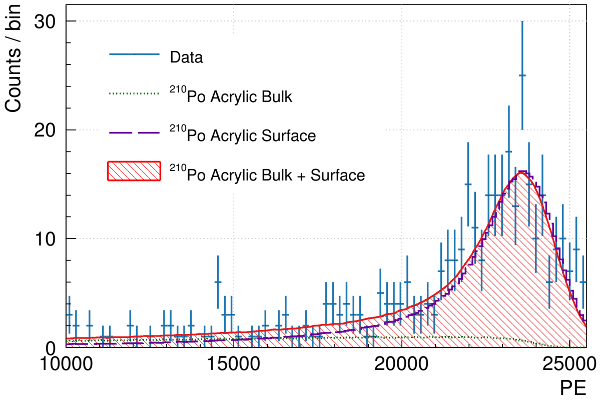

FIG. S6: The ^{210}Po peak in the data overlayed with simulated distributions of contamination present on the acrylic surface (dashed, purple), contamination uniformly distributed in a surface layer of 80 microns depth (dotted, green), and a fit combining both distributions (solid, red). The fit assumes no additional backgrounds in the wide range; therefore the result for the bulk contamination is considered an upper limit.